Materialia 15 (2021) 101020

Contents lists available at ScienceDirect

Materialia

journal homepage: www.elsevier.com/locate/mtla

How the interface type manipulates the thermomechanical response of nanostructured metals: A case study on nickel

O. Renk[a,*], V. Maier-Kiener[b], C. Motz[c], J. Eckert[a,d], D. Kiener[d], R. Pippan[a]

[a] Erich Schmid Institute of Materials Science, Austrian Academy of Sciences, Jahnstraße 12, 8700 Leoben, Austria
[b] Department of Materials Science, Chair of Physical Metallurgy and Metallic Materials, Montanuniversität Leoben, Roseggerstrasse 12, 8700 Leoben, Austria
[c] Saarland University, Institute of Material Science and Methods, Saarbrücken, Germany
[d] Department of Materials Science, Chair of Materials Physics, Montanuniversität Leoben, Jahnstraße 12, 8700 Leoben, Austria

ARTICLE INFO

Keywords:
Interface structure
Boundary character
Nanotwinned
Intergranular stress relaxation
Nanoindentation
Nickel
Rate controlling process

ABSTRACT

The presence of interfaces with nanoscale spacing significantly enhances the strength of materials, but also the rate controlling processes of plastic flow are subject to change. Due to the confined grain volumes, intragranular dislocation-dislocation interactions, the predominant processes at the micrometer scale, are replaced by emission of dislocations from and their subsequent accommodation at the interfaces. Both processes not only depend on the interfacial spacing, but also on the atomistic structure of the interface. Hence, a thorough understanding how these processes are affected by the interface structure is required to predict and improve the behavior of nanomaterials. The present study attempts to rationalize this effect by investigating the thermomechanical behavior of samples consisting of three different interfaces. Pure nickel samples with predominant fractions of low- and high-angle as well as twin boundaries with a similar average spacing around 150 nm are investigated using high temperature nanoindentation strain rate jump tests. Depending on the interface structure, hardness, strain rate sensitivity and apparent activation volumes evolve distinctively different with testing temperature. While in case of high-angle boundaries for all quantities a pronounced thermal dependence is found, the other two interface types behave almost athermal in the same temperature range. These differences can be rationalized based on the different interfacial diffusivity, affecting the predominant process of interfacial stress relaxation.

1. Introduction

The enhanced fractions of grain boundaries (GBs) and interfaces making up nanocrystalline (NC) materials or nanocomposites significantly alter their property spectrum. The tremendous decrease of the mean obstacle spacing for dislocations enhances strength to unprecedented levels [1–4]. Besides that, the rate-controlling processes of plastic flow are altered compared to the coarse grained reference state, as the probability for storage or interaction of defects within the grains or phases diminishes when their volume is reduced to the nanoscale. For FCC metals, this implies a shift from forest cutting (i.e. dislocation-dislocation interactions) to dislocation emission from and interaction with GBs or interfaces [5]. Accordingly, the measured strain rate sensitivity (SRS), m, of plastic flow is significantly enhanced for NC FCC metals, accompanied by a reduction of the (apparent) activation volume, V^*, being only on the order of several 10 b^3 [6–9]. It is evident that the interaction of defects with interfaces strongly depends on their atomistic structure, consequently affecting the resulting properties. Nanotwinned (NT) metals are one of the most prominent examples demonstrating this effect. The introduction of nanoscaled twins into micrometer-sized copper grains allows to unite high strength with excellent tensile ductility [10,11]. This superior property combination is in clear contrast to conventional NC or ultra-fine grained (UFG) copper, offering comparable strength but extremely limited tensile ductility [12,13]. The synergy of strength and ductility in case of NT copper is associated with the simultaneous possibility of easy slip transfer and generation of sessile dislocations at the twin boundaries (TBs). This ensures work hardening capability, not accessible for random high-angle grain boundaries (HAGBs), where dislocations easily annihilate at the opposite GBs [14,15]. Similarly, molecular dynamics (MD) simulations comparing samples with HAGBs and low-angle grain boundaries (LAGBs) suggest a stronger work hardening ability in the latter case [16], in line with experimental observations on aluminum [17,18]. Apart from mechanical properties, also the thermal stability is significantly affected by a change of the interface structure. Nanomaterials with large fractions of LAGBs or TBs showed significantly improved thermal stability compared to structures consisting mainly of HAGBs, rationalized by their reduced interfacial energies and diffusivities [19–22]. This emphasizes that not only the mechan-

* Corresponding author.
E-mail address: oliver.renk@oeaw.ac.at (O. Renk).

https://doi.org/10.1016/j.mtla.2021.101020
Received 20 January 2021; Accepted 22 January 2021
Available online 24 January 2021

ical behavior, but also other properties such as the thermal stability are strongly determined by the interface type. Hence, also the thermo-mechanical response will be readily affected, but has remained widely unexplored so far, especially the case for nanostructures built of LAGBs.

Focusing on the mechanical behavior, the influence of the interface character should be readily reflected in the rate-controlling processes of plastic flow. However, studies unraveling the effect of the interface character and taking a potential size dependence (i.e. effects resulting from the interfacial spacing) into account, remain, except for those on NT copper [14], scarce and are currently mostly limited to ambient temperature. Unexpectedly, a comparison of NT copper with conventional NC copper suggested that the SRS and activation volume V^* of plastic flow do not differ for a given interfacial spacing and follow the same scaling laws [14,23]. Based on their fundamentally different properties discussed above and recent results emphasizing the importance of intergranular stress relaxation [9], this agreement is astonishing. In fact, the measurements obtained on various UFG and NC FCC materials showed that the SRS remained constant at low levels until above a certain temperature a pronounced increase occurred [9]. Above this transition temperature also the apparent activation volumes started to decrease, approaching single digit values, indicative of diffusion-based processes. This is supported by activation energies at elevated testing temperatures being comparable to those reported for GB diffusion [9]. Moreover, the transition temperatures were found to be only 50 – 70 K below the average ones measured for thermally-induced dislocation annihilation at random HAGBs in these particular materials, cf. Refs. [9,24]. Above the mentioned transition point, the temperature seems sufficient to allow for thermally facilitated stress relaxation, reflected in a pronounced temperature and time dependence of plastic flow. As a whole, these results point to intergranular stress relaxation as the controlling process. However, models describing the kinetics of purely thermally-induced stress relaxation (Eq. (1)) [25,26], indicate that apart from material constants such as the shear modulus, G, the atomic volume Ω, the boundary width δ, and fundamental constants such as the Boltzman constant, k_B, and a pre-factor A (reported to be about 1/200 for severely deformed nanomaterials [25,27]), the relaxation time τ_{relax} only depends on the boundary diffusivity D_{GB} and the spreading distance s, which is natively restricted to the grain size as an upper limit.

$$\tau_{relax} = A\,\frac{k_B T s^3}{G\Omega D_{GB}\delta} \tag{1}$$

Based on Eq. (1), it is evident that for a given material and interfacial spacing, the relaxation time mainly depends on the interfacial diffusivity. Accordingly, different relaxation times and hence deformation behavior are expected for different interface types. In other words, different values of the SRS or work hardening rates would be expected, contrasting the mentioned agreement in previous studies [14]. Although the reported similarities between HAGBs and TBs could result from the restriction to ambient testing temperatures, the obvious controversies motivated a detailed study unraveling the effect of the interface type on the deformation behavior of nanostructured metals. Due to its higher melting point we used nickel as a model material to allow for measurements in a wider temperature range without the occurrence of significant microstructural modifications. In addition, NC nickel and nickel alloys have been widely studied at room temperature (e.g. Refs. [8,28–31]) what allows for a comparison with the gathered data. High temperature nanoindentation strain rate jump tests performed on samples with LAGBs, HAGBs and TBs of similar spacing allowed to assess the effect of the interface type on the deformation response and to prove the raised hypothesis that interfacial stress relaxation is the predominant rate-controlling process.

2. Experimental

To understand how the interface type affects the deformation behavior, nanostructured nickel samples with different boundary types but similar interfacial spacing were synthesized. The samples considered in this work consist predominately of HAGBs, LAGBs and TBs, labelled HAGB, LAGB and NT sample hereafter. The HAGB and LAGB samples were processed by high pressure torsion (HPT) and cyclic high pressure torsion (CHPT) at ambient temperature. Nickel (99.99%, from Goodfellow) samples with 10 mm diameter and 1 mm height were deformed by quasi-constrained monotonic HPT [32] at ambient temperature for 10 rotations at a rotational speed of 0.2 rot min^{-1} under an applied nominal pressure of 5.1 GPa. Such severe monotonic strains result in an UFG structure consisting of random HAGBs which make up to 75–80% of the total boundary length [33,34]. To create a nanoscaled structure of similar dimensions but consisting mainly of LAGBS, recrystallized Ni samples (773 K/1 h) having the same dimensions (10 mm diameter and 1 mm height) were cyclically HPT deformed (5° twist angle) for five cycles using a setup introduced earlier [35,36]. The large plastic strain amplitudes applied allowed to create a distinct fraction of dislocation cells having approximately the same spacing as obtained in case of the monotonically deformed samples. The NT nickel samples were synthesized using pulsed electrodeposition. Sheets of several millimeter thickness consisting of NT nickel structures were grown on copper substrates. Butindiol (0.02 g l^{-1}) and sodiumsaccharin (3 g l^{-1}) were added to the electrolyte as grain refiners. A detailed chemical composition of the electrolyte can be found elsewhere [37,38]. Deposition was performed using square pulses with a cathodic current density of 45 mA cm^{-2} and an anodic current density of 65 mA cm^{-2} with a pulse duration of 5 ms, respectively.

Boundary spacings and fractions of boundary characters of the HAGB and LAGB samples were analyzed using an electron backscatter diffraction (EBSD) detector attached to a LEO 1525 field emission gun scanning electron microscope (SEM, Carl Zeiss Microscopy, Germany), while for the NT nickel samples transmission Kikuchi diffraction (TKD) in an on-axis configuration [39] with a setup from Bruker, Germany was used. The step size in case of the TKD scans was set to 10 nm, while 25 nm were used for the conventional EBSD scans. For conventional EBSD, a final electrolytical polishing step (Struers electrolyte A2) was used to remove any deformation layer present from mechanical grinding and polishing. For TKD, an electron transparent NT sample was prepared following standard TEM preparation routines of mechanical grinding, polishing and dimpling, followed by gentle ion polishing. The obtained data was analyzed using a standard software package (OIM analysis 5.3, EDAX). For the HAGB and LAGB samples the microstructures were analyzed in radial (RAD) direction of the HPT disk at a radius of 4 mm, while the NT structure was observed perpendicular to the growth direction. To examine the thermal stability of the samples and to determine the meaningful temperature range for the high temperature nanoindentation protocol used to assess the deformation behavior, the samples were isochronally annealed (30 min) at various temperatures. Vickers microhardness measurements (0.5 gf load, 15 s) at ambient temperature accompanied by microstructural analysis as described before enabled to determine the thermal stability range. Please note that in case of Vickers hardness, not the projected area, but the contact area is considered for evaluating the hardness. Hence, for the same test temperature and material condition, these values are slightly reduced compared to the nanoindentation data. Minor effects could further arise from differences in applied strain rate.

To obtain insights into the deformation behavior, nanoindentation strain rate jump tests at room temperature and elevated deformation temperatures were performed [40]. In case of the HPT disks (HAGB and LAGB samples) the indentation direction was chosen along the axial direction, while the nanotwinned samples were indented along the growth direction, i.e. perpendicular to the TBs. Prior to the tests the sample surfaces were mechanically ground and polished followed by a final electrolytical polishing step (Struers electrolyte A2) to remove any deformation layers. In case of the HPT disks (LAGB and HAGB structures), the indents were performed at a radius of about 4 mm, i.e. where all microstructural investigations were performed. From the nanoindentation

strain rate jump tests hardness, H, strain rate sensitivity, m, and apparent activation volumes, V^*, as a function of the testing temperature can be extracted. Hence, insights into the rate-controlling deformation processes of the different nanostructures and interfaces can be gained. All tests were performed on a platform Nanoindenter G200 (KLA, CA, USA) equipped with a continuous stiffness measurement (CSM) unit. The CSM unit superimposes a sinusoidal load signal (2 nm amplitude and 45 Hz frequency used here) that allows to deduce contact stiffness and thus modulus and hardness continuously throughout the test. For elevated testing temperatures, a laser heating stage (SurfaceTec, Hückelhoven, Germany) was used. Both, the tip and the sample are heated independently, allowing to adjust and stabilize the contact temperature carefully, minimizing thermal drift [41]. Due to the laser heating, the selected temperatures and subsequent stabilization are reached within a few minutes, reducing the exposure prior to the indent. This also guaranteed a well-defined and homogenous temperature distribution throughout the indentation sequence. The whole system including sample tray and the copper cooling shield surrounding the indentation tip was water cooled and the chamber temperature was close to 291 K. An inert gas atmosphere (forming gas – N_2 containing 5% H_2) was obtained by two individual valves that controlled the gas flow around the sample tray and the heated tip. This created an oven-like atmosphere and ensured that oxidation of the samples could be prevented. After the high temperature tests, all samples were inspected visually and, although not quantified, no obvious oxidation was recognized. For all measurements Berkovich tips were used. In case of the elevated testing temperatures sapphire tips (Synton-MDP, Nidau, Switzerland together with Surface Tec, Hückelhoven, Germany) were used to minimize chemical interactions between tip and sample [42], while at ambient temperature diamond tips (Synton-MDP, Nidau, Switzerland) were used. Frame stiffness as well as tip shape calibrations were made on fused silica regularly between the individual samples according to the Oliver-Pharr method [43]. A thermal drift of less than 0.1 nm/s was allowed prior to any test and was determined at each testing temperature before as well as after each array of indents.

At every chosen test temperature at least four indentations, separated by 50 μm, were performed within the heating cycle, ranging between room temperature (RT) and 573 K, depending on the thermal stability of the individual samples, respectively (Ni HAGBs: 298, 373, 398, 425, 448, 473 and 498 K; Ni LAGBs: 298, 373, 423, 473, 498, 523, 548 and 573 K; Ni NT: 298, 373, 398, 423, 448, 473, 498, 523, 548 and 573 K). The nanoindentation tests were performed in constant strain rate-controlled mode [44]. The applied strain rate was altered abruptly after every 500 nm indentation depth, starting with 0.05 s^{-1}, reducing it further to 0.01 s^{-1}, increasing it back to 0.05 s^{-1}, dropping to 0.005 s^{-1} before jumping back to the initial strain rate of 0.05 s^{-1}. All hardness and modulus data reported in the following are averaged values obtained at a strain rate of 0.05 s^{-1} between 1050 and 1450 nm indentation depth. Based on the strain rate jump tests, the strain rate sensitivity, m, and the apparent activation volumes, V^*, can be calculated according to Eqs. (2) and (3) [30], respectively, where H denotes the hardness, $\dot{\varepsilon}$ the strain rate, C^* a constraint factor being 2.8, k_B the Boltzman constant, and T the absolute temperature.

$$m = \frac{\partial(\ln(H))}{\partial(\ln(\dot{\varepsilon}))} \tag{2}$$

$$V^* = \frac{C^* * \sqrt{3} * k_B * T}{m * H} \tag{3}$$

It should be noted that the values calculated according to Eqs. (2) and (3) could depend on the applied strain (i.e. indenter geometry) and strain rate, with the latter chosen rather high within this study. Notably, for high strain rate tests constant hardness (flow stresses) prior to another strain rate jump may not always evolve, complicating this analysis. This was, however, not the case here, as for the majority of the applied rate jumps rather constant hardness levels evolved, compare Fig. 6b. Furthermore, while the dislocation density can affect the calculated SRS or V^* values for metals subjected to comparably low strains [45], this issue is not pronounced for nanostructured materials tested here. Previous results indicate that Berkovich tips imposing a strain of ~7% strain already necessitate a large number of dislocations. Thus, no significant difference of the SRS or V^* at a given temperature was evidenced, independent if measured during the heating or cooling sequence (i.e. testing already a relaxed state) [9].

As the test protocol includes two strain rate jumps back to a previous strain rate ($\dot{\varepsilon} = 0.05\ s^{-1}$), the hardness-contact depth curves can be used as a first indicator for structural modifications due to the thermomechanical exposure of the nanostructures. As will be detailed later, for HAGB samples tested at specific temperatures, these curves already suggested grain growth beneath the indenter tip. Therefore, the cross-sections of particular indents were extracted and inspected as well. After depositing a protective platinum layer on top of the indent using a gas injection system in a focused ion beam (FIB) workstation (Zeiss Auriga, Zeiss, Germany), a slice through the residual impression with a thickness of about 2 μm was extracted from the sample using an Omniprobe 200 micromanipulator (Oxford Instruments, UK). Subsequently, the samples were attached to a copper grid by platinum deposition and analyzed using conventional EBSD as specified before.

All residual imprints were further imaged using a Keyence laser scanning confocal microscope to determine the height of the pile-ups and their evolution with temperature. The recorded data was analyzed using the software package Gwyddion 2.56. Linear profiles were applied to the imaged indents to measure the pile-up heights. The reported values are averages with the standard deviation as the error bar. It should be noted that for some conditions (test temperature, interface type) the error bar seems rather large, which is not a result of pronounced scatter between the indents taken at a given temperature, but rather due to distinct deformation differences between the three faces of the Berkovich tip.

3. Results

3.1. Microstructural characteristics and thermal stability of the three different types of nickel samples

Fig. 1 shows representative micrographs of the three different types of nickel samples under investigation. The HAGB samples (monotonically HPT deformed, Fig. 1a) exhibit a typical UFG microstructure with slightly elongated grains along the tangential (TAN) direction, consisting predominantly of HAGBs with fractions of up to 75% of the total boundary length. It should be mentioned that after severe straining no preferred misorientation angle or axis pair can be determined, as reported earlier [33,34,46,47]. Thus, the generated HAGBs can be considered as random. This is also evident from the misorientation distribution, Fig. 2a. Average boundary spacings were determined using the line intercept method and setting a critical misorientation angle of more than 15°, yielding average minimum dimensions (along the axial direction) of about 190 nm. The LAGB samples (Fig. 1b) appear similar to conventional cold-worked structures. Inside the still distinguishable coarse grains, well-defined dislocation boundaries with low misorientation angles developed. The fraction of boundaries with a misorientation angle below 15° in these samples makes up 75% of the total boundary length. Because the average spacing of the LAGBs was determined by conventional EBSD, the threshold angle to identify a grain was set to 2°, although dislocation boundaries with an even lower misorientation angle may exist. Accordingly, the average spacing along the axial direction (minimum dimensions) determined for this condition (265 nm) can only be considered as an upper bound for the actual spacing. For both, the HAGB samples and the LAGB samples, dislocation-based plasticity is evident from the ODF sections, which show a good agreement with the ideal texture components [48] in Fig. 2c. The NT nickel samples consist of columnar grains in growth direction, having an average

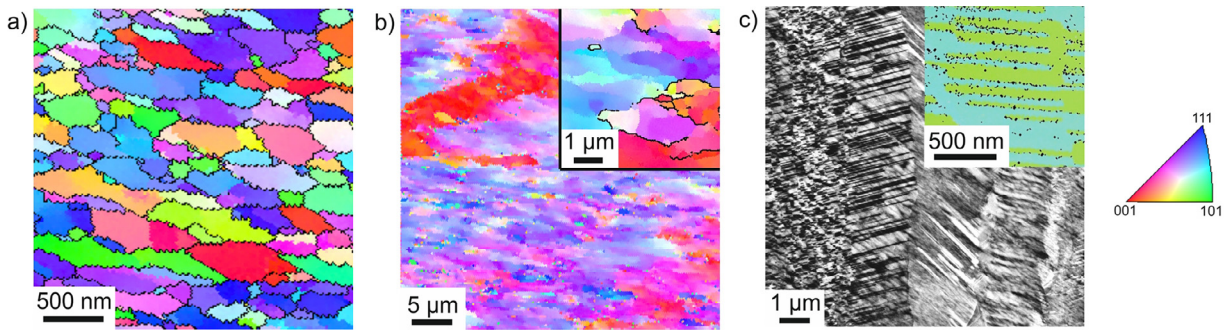

Fig. 1. Representative microstructures of the tested nickel samples having three distinct interface types. (a) HPT deformed nickel consisting predominantly of HAGBs; (b) Recrystallized and cyclically cold-worked nickel with a majority of LAGBs (boundaries in the inset image in black denote HAGBs), and (c) electrodeposited NT nickel. For all specimen types the average interfacial spacing is with 150–250 nm rather similar.

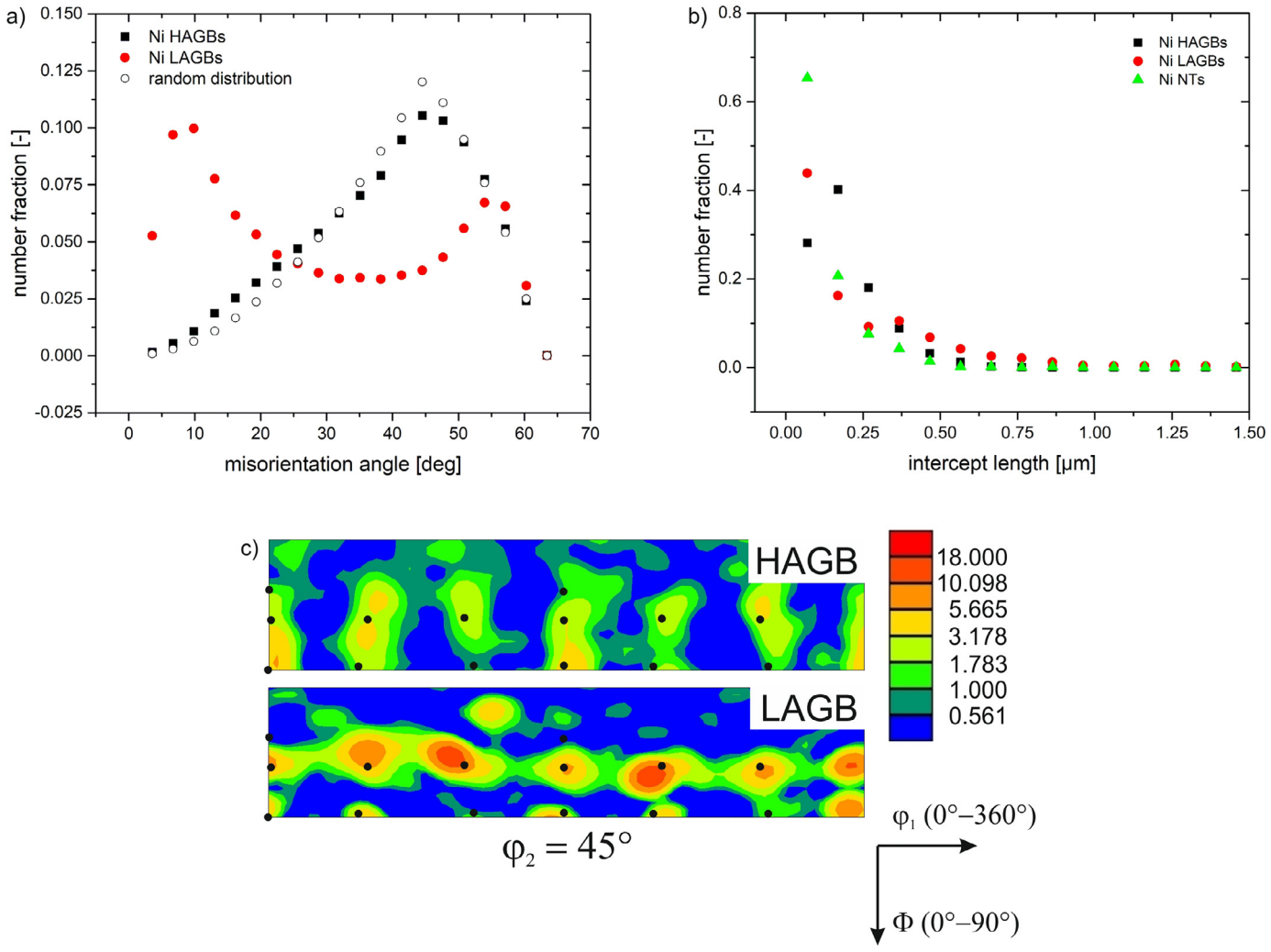

Fig. 2. (a) Uncorrelated misorientation distribution of the HAGB and LAGB samples synthesized by HPT and cyclic HPT, respectively, with the random distribution (open circles) given for comparison; (b) distribution of the line intercepts for the different interface types; (c) Representative ODF sections of the HAGB and LAGB samples with the black dots indicating the position of ideal texture components expected for dislocation-based plasticity [48].

thickness of about 2.5 µm, with the largest ones being up to 10 µm thick. Inside the columnar grains high densities of twin boundaries can be found, see Fig. 1c. This results in a {111} fibre texture in growth direction. The majority of the twin boundaries are coherent twin boundaries (fraction ~ 85%) and their average spacing based on line intercepts is about 120 nm. Thus, samples with relatively similar boundary spacings could be synthesized and assessed with respect to their mechanical properties and thermal stability. It should be noted that the purity of the NT nickel samples is lower compared to the other two interface types, with sulphur being known as main impurity in ED nickel samples. However, as the preferred segregation sites are the columnar HAGBs, rather than the closely spaced TBs which determine the mechanical properties, this is not expected to cause an effect, compare Ref. [49].

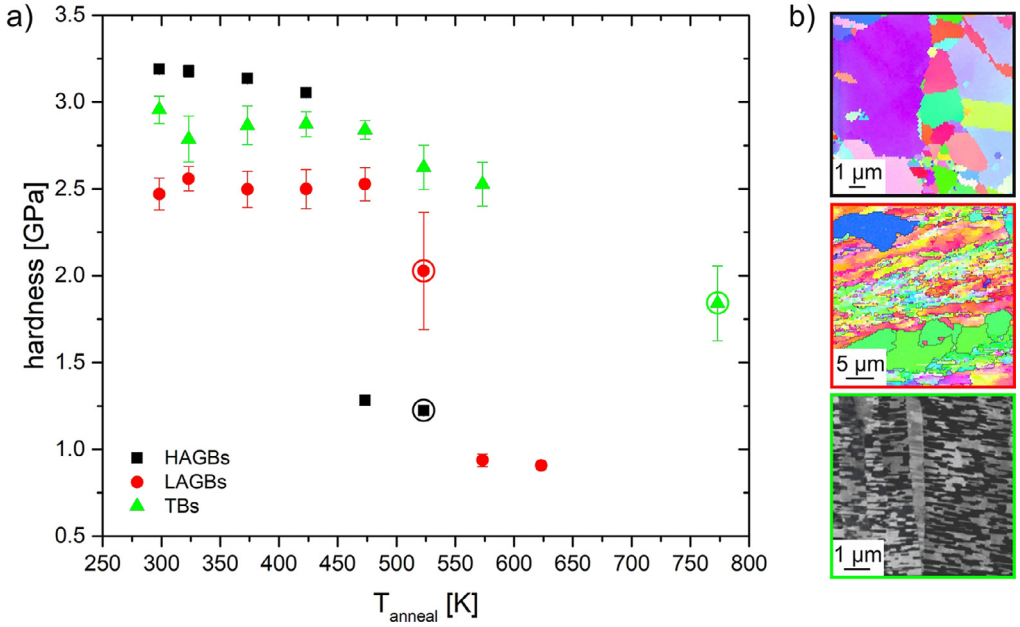

Fig. 3. Thermal stability of the three different nickel microstructures as revealed from room temperature Vickers microhardness (0.5 gf load) tests performed after isochronal (30 min) annealing and complementary microstructural investigations. Circles correspond to the images in b). Data of the HAGB specimens is taken from Ref. [50]. Please note that the difference of the RT hardness compared to Fig. 6 originates from the use of the contact area instead of the projected area to determine the Vickers hardness.

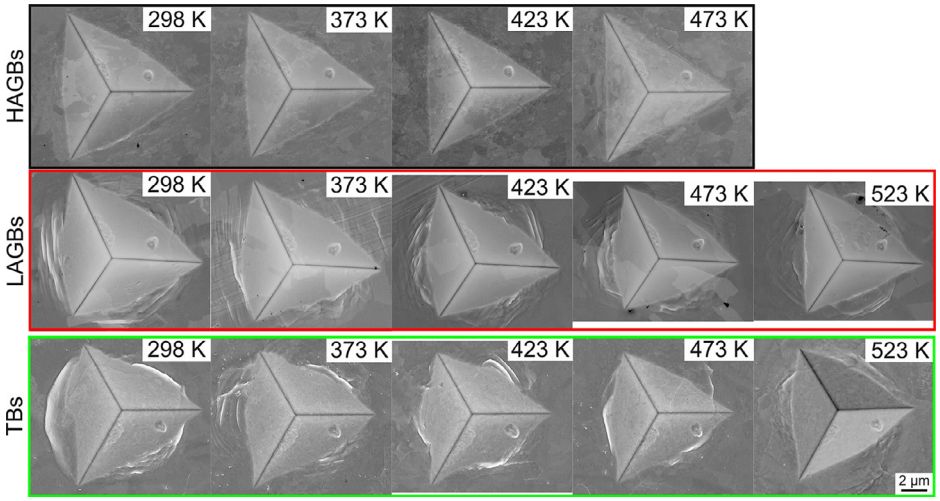

Fig. 4. Representative SEM images of the indents; samples containing HAGBs (upper row), LAGBs (middle row) and TBs (bottom row) at indicated testing temperatures.

A similar boundary spacing for all three types of specimens is also evident from the hardness measurements taken at room temperature. For all different types of specimens a comparable hardness of 2.5–3.2 GPa was measured, see Fig. 3. To test their thermal stability, the samples were subjected to isochronal (30 min) annealing treatments at different temperatures. Vickers microhardness measurements at room temperature accompanied with structural characterization allowed to determine any structural changes. These thermal stability limits were used to set the testing temperature range for the nanoindentation experiments. It can be noticed that the HAGB samples have a significantly lower thermal stability compared to the LAGB and TB samples. Already above temperatures of 423 K massive grain growth occurred for the HAGB specimens, while at this temperature pronounced changes still remain absent for the LAGB and TB specimens. At annealing temperatures of 523 K also in the LAGB samples first recrystallization nuclei can be observed (Fig. 3b), explaining the rather large standard deviation of hardness for this particular annealing condition. At this annealing temperature the hardness slightly drops also in case of the NT samples, but changes of the TB spacing remain small. Even after annealing at 773 K, the TB spacing remains well below a micron, indicating a superior thermal stability. The improved thermal stability in case of the LAGB and TB specimens compared to the HAGB samples is in line with investigations on NT copper [20,21] and nanolaminated nickel consisting of nanoscaled LAGBs [19]. It can be rationalized by their lower interfacial energy and diffusivity compared to general HAGBs, consequently reducing the driving forces for growth and the atomic mobility within the interfaces [19,22]. Apart from thermal stability, pronounced differences between the three different types of nickel samples are also evident when considering their mechanical behavior, as will be outlined in the following section.

3.2. *Deformation behavior at ambient and elevated temperatures*

Already from the shapes of the remanent impressions after room and elevated testing temperatures, a distinctively different deformation behavior for the three interface types is evidenced. Representative SEM images of the indents from the three different types of samples at different

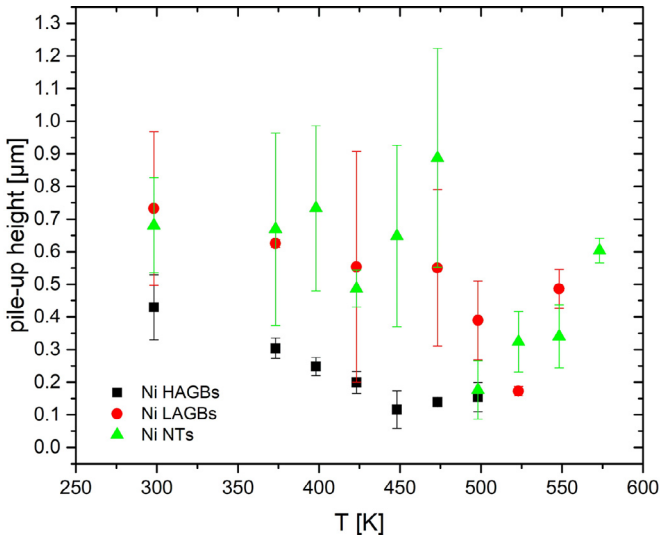

Fig. 5. Analysis of the pile-up height of the different nickel samples as a function of temperature. The large error bars for the LAGB and TB samples are just a consequence of the difference of the pile-up height along the three sides of the Berkovich tip.

testing temperatures are presented in Fig. 4. It should be noted that the micron-sized grain structure visible in some images is just a consequence of recrystallization occurring in the sample, which was continuously heated during the indentation sequences and certainly does not affect any interpretation. For all three interface types, distinct pile-up formation (i.e. a convex deviation from the ideal indent shape) occurs during indentation at room temperature. This is expected for materials having already high strength and, accordingly, limited work-hardening capability [51,52]. Quantitative analysis of the indents (Fig. 5) revealed that for all testing temperatures pile-up formation is more pronounced when LAGBs and TBs are involved. The large error bar for these two samples is not caused by scatter between multiple indents taken at a given temperature, but by the pronounced difference of the pile-up height along the three sides of the Berkovich tip. Up to temperatures of 475 K, the pile-up height of the LAGB and TB specimens is more or less constant, before reducing to lower levels. In contrast, the pile-up height measured on the HAGB specimens already decreased at much lower temperatures, Fig. 5. At testing temperatures of 423 K, still below the thermal stability limit, the indents resemble already an almost perfect and straight shape, with the pile-up height being similar to the ones taken at 473 K where grain growth already occurred.

Apart from the clear differences of the indent shapes for the three sample types and their evolution with temperature, also the temperature dependence of the measured hardness values exhibits quite different trends. While for the samples containing LAGBs and TBs the hardness does not change significantly with an increase of the testing temperature, the HAGB sample shows a distinct temperature dependence, see Fig. 6a. Data taken from Ref. [9] obtained on a UFG Ni4.5Al alloy consisting predominantly of HAGBs is added for comparison. As for the pure nickel sample with HAGBs also for the alloyed variant the hardness is extremely temperature sensitive. The alloying content only shifts the testing temperatures that cause a substantial drop in hardness towards higher values. Although measuring well below the thermal stability limit ($\sim 0.25\ T_m$), the hardness of the HAGB samples decreases already remarkably. Because both, the LAGB and NT samples do not show a distinct temperature dependence, above $\sim 0.22\ T_m$ the hardness of these two specimens exceeds those of the HAGB samples. However, it is well-established that nanostructures consisting predominantly of HAGBs are prone to grain growth during deformation, even under cryogenic conditions, as evidenced for a variety of testing temperatures and deformation modes, see for instance Refs. [36,53–58]. Therefore, grain growth in case of the HAGB samples may already occur below the thermal stability limit due to the deformation (7% equivalent strain) imposed by the Berkovich indenter, explaining the reduced hardness values with increasing testing temperature. As the indentation protocol consisted of a series of strain rate jumps, including two jumps back to a previous strain rate, the recorded hardness-contact depth curves (Fig. 6b) already allow to deduce microstructural instabilities. Nevertheless, from the hardness-contact depth data, this is not expected up to testing temperatures of 398 K, since for testing temperatures below 398 K, a strain rate jump back to a previous strain rate (i.e. 0.05 s^{-1}) always leads to identical hardness levels, indicating microstructural stability. This is different for higher testing temperatures. Already at 423 K, the hardness for the last strain rate segment remains below the ones obtained in the previous two segments, presumably already a consequence of measuring close to the thermal stability limit.

However, already for testing temperatures of 398 K, where the hardness-contact depth signal suggests a stable microstructure, the hardness differs already more than 30% compared to room temperature. To elucidate the reasons for this hardness reduction, another HAGB sample was prepared and indented at 398 K. A lift-out of a thin lamella through the indent performed at 398 K was taken and the volume beneath the indent subsequently analyzed. The obtained backscattered electron images and detailed color IPF maps of the microstructures are shown in Fig. 7. Obviously, the grain size beneath the indent is significantly larger than in unaffected regions further away. On a closer look the region where noticeable grain growth occurred is limited to a circular shape around the indent. Estimating the plastic zone size according to Refs. [59,60] indicates that grain growth is confined to this volume, highlighted by the dashed line. Despite the indentation-induced growth is significant, it is not reflected in the hardness-contact depth curves, showing identical hardness levels for a jump back to the same strain rate (i.e. 0.05 s^{-1}). This could be related to the fact that for the self-similar Berkovich indent the realized equivalent strain and, hence, the amount of growth is independent of the penetration depth, but just the size of the plastic zone increases.

3.2.1. *Strain rate jump tests*

From the high temperature nanoindentation tests, strain rate sensitivity, m and apparent activation volumes, V^*, were determined as a function of temperature according to Eqs. (2) and (3). The values reported in the following are averages, with the standard deviation as the error bar. Fig. 8 summarizes these quantities for the three different specimen types as a function of the test temperature. In addition, data obtained on a NC Ni4.5Al alloy consisting of a majority of HAGBs (Ref. [9]) is plotted for comparison. As for hardness and indent morphology, also the temperature dependent trends of strain rate sensitivity and apparent activation volume differ remarkably for the three interface types investigated. Again, these trends are comparable for the LAGB and NT specimens but differ substantially for the HAGB samples, Fig. 8a. At ambient temperature, SRS is low (0.01 – 0.02) and rather similar for all three interface types, although slightly higher values were measured for the HAGB nickel and Ni4.5Al samples. Already for slightly elevated testing temperatures, the differences between the samples become apparent. While for the pure nickel samples with HAGBs the SRS quickly increases with temperature, the LAGB and NT specimens behave rather athermal. This also holds true for the alloyed nickel sample consisting predominantly of HAGBs. However, similar to the pure nickel HAGB samples, above $\sim 0.25\ T_m$ the SRS of the Ni4.5Al alloy quickly increases. In case of the pure nickel HAGB samples, the SRS reaches values of about 0.05 at 423 K, before decreasing again. This drop of the SRS can be attributed to the occurrence of significant grain growth, as the testing temperature exceeded the thermal stability of the samples, Fig. 3. Even higher values of 0.1 can be measured in case of the Ni4.5Al HAGB samples, although for a given temperature the SRS of the pure nickel samples is always higher. In contrast, for the LAGB and NT samples, no change of the SRS

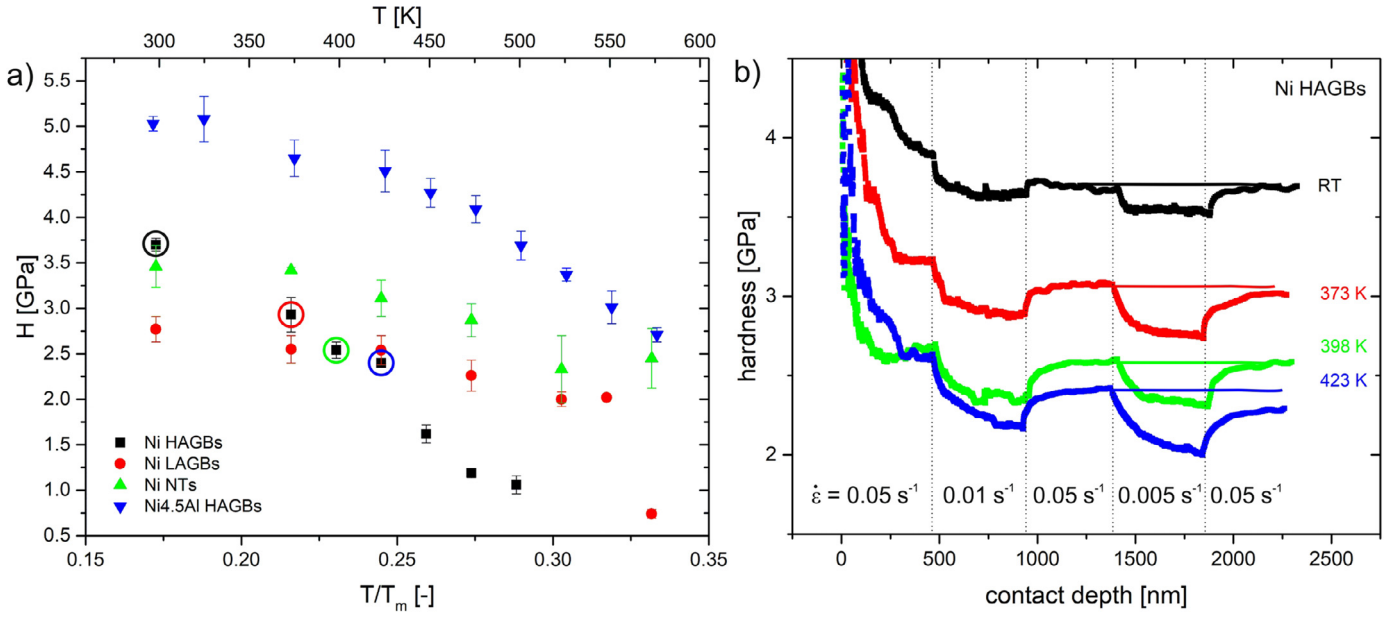

Fig. 6. (a) Hardness as a function of testing temperature for nickel samples with different types of interfaces. Data obtained on a NC Ni4.5Al alloy (Ref. [9]) with a predominant fraction of HAGBs is added for comparison. Circled data points in (a) refer to the hardness-contact depth curves of the HAGB samples displayed in (b).

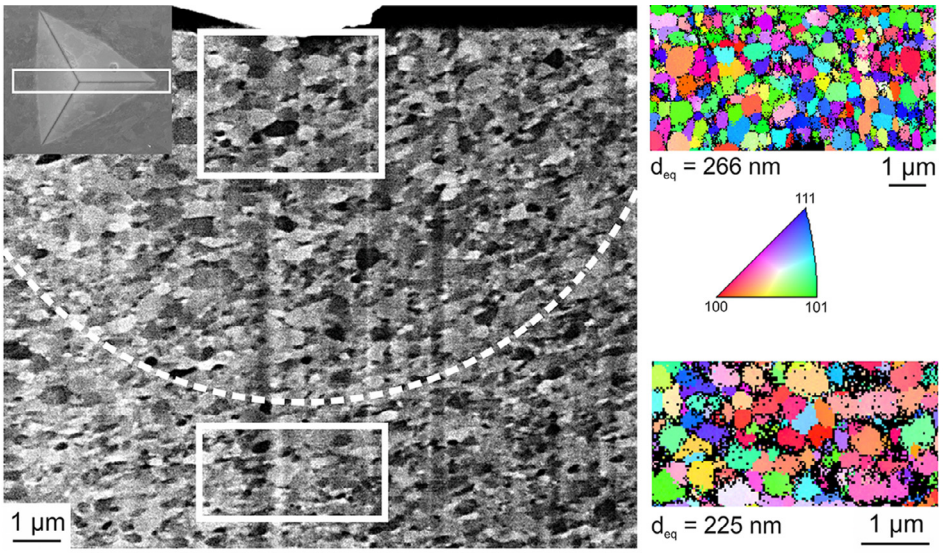

Fig. 7. Backscattered electron image showing microstructural changes beneath an indent of a HAGB sample indented at 398 K. The dashed line corresponds to the maximum depth of the plastic zone, estimated according to Refs. [59,60]. Please note the different scale bars of the images.

could be measured up to temperatures of 473 K (~ 0.25 T_m). Even for higher testing temperatures, the increase remains rather small and for both types of samples within the whole temperature range tested, the SRS exceeds only slightly that measured in case of HAGBs already at ambient temperature ($m \sim 0.02$). Nevertheless, also for these two interface types a similar trend as measured for the HAGB samples can be expected, given that the structures remain stable up to way larger temperatures than tested here. This is supported by data obtained during large strain deformation of pure coarse-grained nickel (i.e. in compression and torsion), suggesting that at least temperatures of 873 K would be required to measure a distinct rate dependence of flow stress [61,62]. While this would be possible for the NT samples (compare Fig. 3), in case of the LAGB samples recrystallization occurred already at about 0.32 T_m and caused a drop of the SRS to even lower values.

As can be expected for nanostructures, the apparent activation volumes V^* are on the order of several tens of b^3 for all specimens tested at room temperature, see Fig. 8b. With ~ 40 b^3 the apparent activation volumes in case of the LAGB and NT specimens are slightly larger than the ones calculated for the HAGB samples. For the pure and alloyed HAGB samples, values of about 20 b^3 were measured. As the SRS of the LAGB and NT samples does not change significantly with temperature according to Eq. (3), the apparent activation volumes of these samples increase moderately up to about 60 b^3 with testing temperature. Significantly larger values of almost 400 b^3 are measured for the LAGB specimen after recrystallization, as expected for a coarse-grained FCC metal at moderate testing temperatures, with forest cutting being the rate controlling process. In contrast, V^* of both, the pure and alloyed HAGB specimens, remains rather constant before starting to decrease once reaching the temperatures where the SRS quickly increases. This trend of decreasing V^* is restricted to a narrow temperature range in case of the pure nickel HAGB samples as grain growth occurs, reflected in a distinct increase of the activation volume. However, in case of the

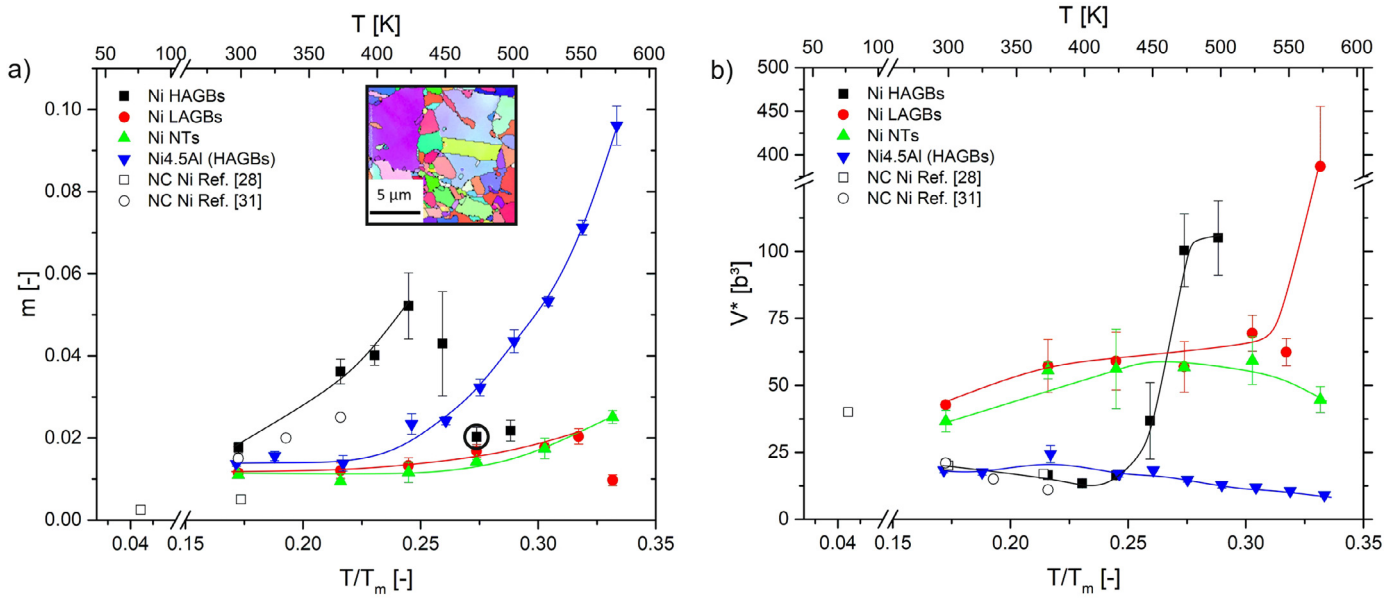

Fig. 8. (a) Strain rate sensitivity, m, and (b) apparent activation volume, V^*, of the nickel samples having different interfaces as a function of testing temperature. Data for a NC Ni4.5Al alloy (Ref. [9]) consisting predominantly of HAGBs and ED NC Ni (Refs. [28,31]) are added for comparison. Trend lines are added as guide for the eye.

more stable Ni4.5Al HAGB samples, the decrease is clearly visible and single digit activation volumes, indicative for diffusive processes, are approached, Fig. 8b.

Based on the measured hardness and activation volumes, the apparent activation energies of the rate limiting processes can be estimated according to Eq. (4) [63]. This approach describes the activation barrier, Q, as stress-dependent Gibbs free energy, ΔG, to activate plastic flow. Since it is generally assumed that contributions from the entropy term are negligible [29,64], ΔG is closely related to the activation enthalpy ΔH_{act}, expressed as:

$$Q \sim \Delta H_{act} = \frac{H V^*}{\sqrt{3}\, C T} \frac{\partial(\ln H)}{\partial\left(\frac{1}{T}\right)} \tag{4}$$

with H and V^* being the hardness and apparent activation volume, respectively, T, the absolute temperature and C a constraint factor of 2.8. As can be seen from Fig. 9a, for all three interface types the logarithm of the hardness as a function of the inverse temperature can be reasonably described by a linear fit within two distinct temperature ranges. In case of the HAGB samples, only the one at lower temperatures was considered further, as that at higher temperatures already corresponds to a (partially) coarsened microstructure, compare Figs. 6 and 8. The calculated activation enthalpies and their change with testing temperature are displayed in Fig. 9b. For the HAGB specimens at RT an activation enthalpy of about 2 eV can be determined, which immediately decreases to about 1 eV with an increase of the test temperature. For the LAGB and NT samples, activation enthalpies of about 3 eV are derived at elevated testing temperatures, where properties become slightly temperature dependent. These values are comparable to those expected for GB diffusion (~ 1 eV) and bulk diffusion in nickel (~ 3 eV), respectively, compare Refs. [65,66].

4. Discussion

4.1. Effect of the interface type and the deformation temperature on the indent shape

Distinct differences are not only observed for the mechanical properties, but already for the indent shapes, Fig. 4. While pile-up formation for high strength materials with low work-hardening capacity is expected [51,52], the differences between the three types of samples (Fig. 5) need to be briefly discussed in the remainder. Although LAGBs and TBs are known to have higher work-hardening rates compared to HAGBs [10,13], larger pile-ups are formed for these two samples. Moreover, pile-up formation in case of the HAGB samples continuously diminishes with increasing testing temperature, which is unexpected given the reduction of hardness and work-hardening rate with temperature [51].

Independent of the sample type, due to fixed geometry and indentation depth a consistent volume of material needs to be displaced by the indenter tip. However, this occurs more localized in case of the LAGB and NT samples, presumably because these interfaces are more rigid compared to the HAGBs. While more detailed studies are required to assess this issue in detail, investigations on NT copper support this notion [67]. As detailed in the next chapter, detwinning and local collapse of the twin structure was reported, favoring local plastic flow, hence larger pile-up heights. As the mechanical properties in case of the LAGBs and TBs are largely unaffected by the test temperature, a pronounced change of the pile-up height is thus not expected. In contrast, thermomechanically induced migration of the HAGBs can easily occur (Fig. 7). This is in line with detailed observations showing that at low homologous temperatures under an applied stress field, for a given GB crystallography, HAGBs migrate much faster than LAGBs do [68]. As any moving interface realizes plastic strain, the easier migration of HAGBs could facilitate a more homogenous plastic flow over larger volumes, leading to smaller pile-ups heights. The large affected zone beneath the indent at moderate testing temperatures together with the enhanced rate sensitivity in case of the HAGB specimens (Fig. 7 and Fig. 8) support this picture and also explains the further diminishing pile-up height with increasing test temperature.

Apart from a larger average pile-up height in case of the LAGB and NT specimens, also the height difference between the three faces of the Berkovich tip, giving rise to the large error bars in Fig. 5, is more pronounced. This can be rationalized by two factors. First, for these two specimens, only a single crystallographic orientation is probed (i.e. the size of the grain containing the rigid interfaces is much larger than the volume affected by the indent). Indentation studies on single crystals indicate that the orientation of the facets of the indenter tip with respect to the available slip systems determines the anisotropy of the pile-up

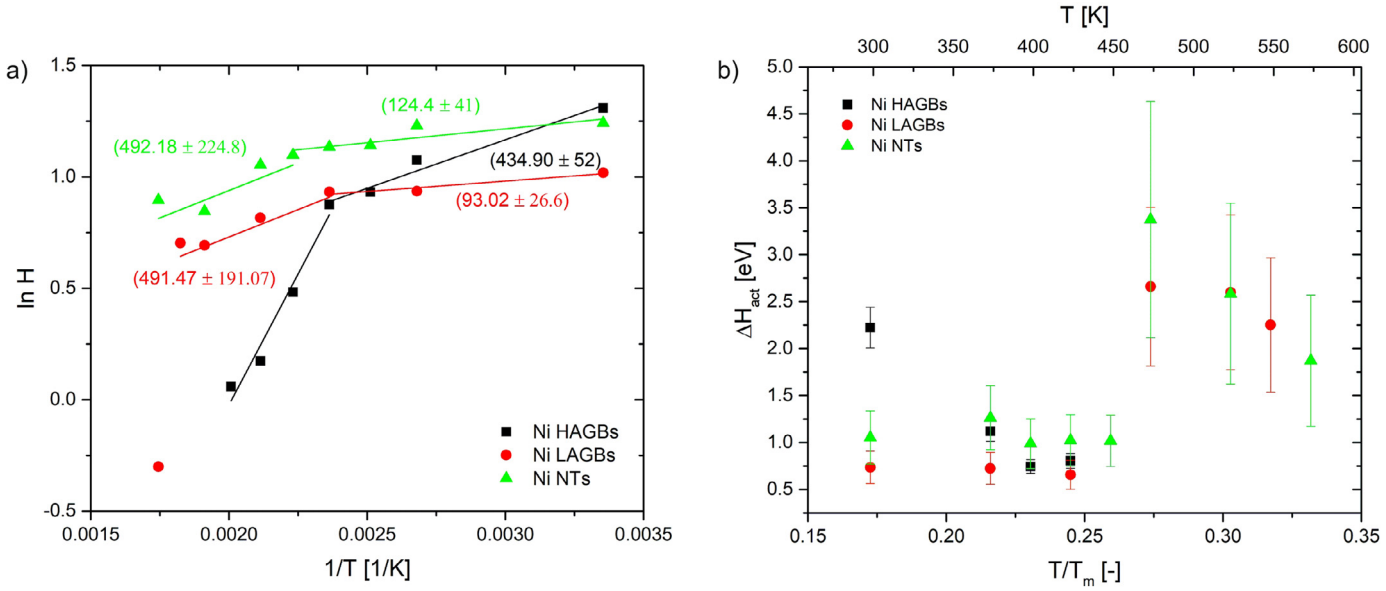

Fig. 9. (a) Plot of ln H (hardness) as a function of the inverse temperature, with slope of the linear fits in the respective temperature intervals displayed. (b) Calculated activation enthalpies, ΔH_{act} as a function of test temperature for the three interface types.

height [69–71]. This anisotropy might be enhanced if additionally interfaces restricting plastic flow are introduced [71], especially if they are perfectly aligned and hardly mobile as the LAGBs and TBs investigated here (i.e. parallel to the shear direction or perpendicular to the growth direction, respectively). However, as the pronounced anisotropy diminishes somewhat at elevated testing temperatures, the effect of the interface seems more important.

4.2. Pronounced temperature dependence of mechanical properties in case of HAGBs

Beside the different appearance of the indent shape, the presented results also reveal, depending on the interface type, a distinctively different thermomechanical response, cf. Figs. 6 and 8. Already the hardness values measured at RT indicate that not solely the interfacial spacing, but also the interface type plays a predominant role in determining the mechanical response. Although the average spacing of the TBs was smaller than that of the HAGBs, the RT hardness of the HAGB specimens was the highest, see Fig. 6a. Based on previous research, this can be explained by (partial) collapse of the NT structure. Strain induced detwinning was clearly observed beneath nanoindents performed on NT copper, with detwinning becoming more pronounced for higher equivalent strains applied [67]. Further, for NT structures a huge anisotropy of the flow stress can be measured, differing by a factor of three between the hard and soft testing modes for NT copper [72]. Although less pronounced, such anisotropic flow behavior was also reported for metallic nanolaminates [73,74]. Beneath the indents bending or realignment of the layers and/or shear band formation was frequently observed [75–77]. Alignment of the layers with respect to the faces of the indenter corresponds to the weakest testing direction, thus facilitates plastic flow. Converted hardness values (using a conversion factor of three) yielding results close to the uniaxial flow stress of the weakest testing orientation, further support this picture. Hence, the slightly lower hardness values measured in case of the NT nickel are most likely a consequence of such instabilities occurring during indentation.

With increasing testing temperature, the differences between the individual sample types become even more pronounced. While the LAGB and NT samples behave quite similar and their properties are only weakly temperature-dependent, the same properties vary strongly with temperature in case of the HAGB samples. As can be noticed from the Ni4.5Al HAGB sample, this pronounced temperature dependence cannot be avoided by alloying, but just the temperatures where pronounced changes occur are shifted towards higher values with alloying content, cf. Figs. 6a and 8. This emphasizes that already at comparably low temperatures of ~ 0.2 T_m, mechanical properties are not solely determined by the average interfacial spacing, but the interface type plays a decisive role. This strong temperature dependence of hardness in case of the HAGB samples is unexpected for FCC metals that conventionally have a temperature-independent yield stress [78–80]. Although due to the temperature dependence of the work hardening rate the flow stresses determined at larger strains can differ substantially also for FCC metals [80], this is not expected for severely deformed materials having already a negligible work-hardening capacity. Moreover, considering the limited equivalent strains realized with the Berkovich tip (i.e. ~ 7%), a decrease of hardness by more than 30% while marginally increasing the testing temperature from 0.17 T_m to 0.23 T_m would not even be expected for a FCC material with a pronounced work-hardening rate [80].

The pronounced temperature dependence of hardness is also evident for the alloyed Ni4.5Al HAGB samples (Fig. 6), in perfect agreement with literature findings on various nanostructured materials, but also for nanocomposites or nanolaminates [28,31,81–85]. The same holds true for metallic thin films, usually composed of NC grain structures. Early nanoindentation studies already reported a reduction of hardness by more than 50% when the testing temperature for gold or copper thin films was increased from RT to 400 K, although the microstructures were claimed to be thermally stable up to this point [86], similar to what was found in the present study. Contrary, the hardness of the LAGB or TB samples remains almost unaffected (i.e. reduction by 8%) in the same testing temperature interval. This suggests that the distinct temperature dependence of the flow stress has its origin in the presence of large fractions of random HAGBs or interfaces. A strong temperature dependence in case of the HAGB samples is, however, also evident for the other properties determined. SRS of the HAGB specimens shows independent of purity a pronounced increase with temperature, accompanied by a drop in the apparent activation volume, V^*, as long as the microstructure remains stable, Fig. 8. In contrast, the SRS values of the LAGB and NT specimens are almost athermal (Fig. 8a), causing together with the almost constant hardness slightly increasing activation volumes with increasing temperature. Focusing on the HAGB specimens, it appears that pronounced property changes of H, m and V^* with tem-

perature occur at similar testing temperatures, suggesting a common origin, cf. Figs. 6 and 8. From the deformation textures (Fig. 2) of the LAGB and HAGB samples and detailed results on NT metals (e.g. Refs. [72,87,88]), it is evident that for all samples dislocation-based plasticity prevails. Hence, as the deformation mechanism remains the same for all three types of samples, the differences in the mechanical behavior need to originate from a change of the interaction of dislocations with the respective interfaces. The strong temperature dependence of properties in case of HAGBs seems to be a peculiarity of the interaction of dislocations with them, occurring only at much higher temperatures in case of interfaces consisting of dislocation arrangements (LAGBs) or almost atomically sharp interfaces such as TBs.

Interactions of dislocations with different interfaces have been studied previously, and given the necessary temperature and/or applied stress, lattice dislocations can enter a GB, forming an extrinsic grain boundary dislocation (EGBD), i.e. a dislocation being not part of the GB structure but coming from outside the GB [26]. Various processes can be coupled to the absorption of an EGBD, such as dislocation emission, GB migration or grain rotation, just to name a few [26]. Although the actual processes can differ depending on boundary crystallography and the Burgers vector of the incoming dislocation [26,87,89,90], this aspect is not considered in the remainder because individual interaction events are not accessible with the experiments used in this work. Nevertheless, probing multiple boundaries of a given type at the same time allows to draw conclusions about their average behavior and respective distinctions. In any case, after the injection or absorption of a lattice dislocation, the GB will be in a state of higher energy. Even in the case of direct transmission, a residual Burgers vector could be left at the interface, if those of the in- and outbound dislocations differ. Consequently, the interface aims at reducing its energy again by intergranular stress release, involving thermally activated processes. These processes determine the behavior of polycrystals to a great extent, as dislocation emission, GB migration or grain rotation are closely related to them [26]. Indeed, our recent study focusing on UFG/NC FCC metals reported good agreement between the average temperatures for thermally-induced dislocation annihilation in random HAGBs with those where SRS increased to remarkably high values [9]. The same holds true for the nickel samples tested here. Average annihilation temperatures for dislocations in HAGBs of pure nickel of about 490 K were reported [24], agreeing reasonably well with the temperatures where maximum rate sensitivity and initiation of grain growth occurred, compare Fig. 8. It should be noted that the increasing temperature dependence of properties in the HAGB samples already below 490 K is not contradicting this idea. As the accommodation of dislocations at GBs and the associated relaxation of their stress fields involve thermally activated processes, the thermal energy required can be reduced by the presence of mechanical stresses, compare Eq. (5). There, G denotes the Gibbs free energy, F the Helmholtz energy, τ the resolved shear stress and V the (physical or real) activation volume of the process [91].

$$G = F - \tau V \tag{5}$$

Accordingly, part of the energy can be provided by the mechanical work done by the applied shear stress, while models describing the kinetics of intergranular stress relaxation (i.e. Eq. (1)) or the mentioned temperatures for dislocation annihilation [24] just consider the pure thermally driven case. Hence, the applied stresses during indentation can significantly reduce the required thermal contributions to overcome the activation barrier. This was indeed observed in *in-situ* TEM straining experiments on UFG aluminum, where the dislocation contrast at the GBs decreased more rapidly when small dislocation pile-ups, i.e. locally higher resolved shear stresses, were present [92]. This is in line with the development of a pronounced temperature dependence already below the average annihilation temperatures reported.

However, despite considering the thermal part only, the mentioned models describing the kinetics of interfacial stress relaxation can still be used to qualitatively rationalize the obvious differences between the HAGB and the LAGB/NT samples, as the applied stress is roughly the same for all three interface types. As stated previously, the required relaxation time depends mainly on material properties (i.e. shear modulus, atomic volume, interfacial spacing and width) and interfacial diffusivity [25,26], cf. Eq. (1). Considering that the nickel samples tested here have a quite similar boundary spacing and assuming a rather constant boundary width, the only parameter that fundamentally differs is the interfacial diffusivity. For the LAGB and NT samples, the activation energies for boundary diffusion are expected to be similar to bulk diffusion, i.e. a difference by a factor of about two compared to the HAGB specimens [93]. Available interfacial diffusion data for nickel along deformation-induced LAGBs [22] and HAGBs [27] at temperatures close to the highest ones tested here yield values of $D_{\mathrm{LAGB\ (458\ K)}} = 5.14\times10^{-19}$ m^2 s^{-1} and $D_{\mathrm{HAGB\ (440\ K)}} = 5.03\times10^{-17}$ m^2 s^{-1}, respectively. For comparison, the bulk diffusivity at this temperature would be only on the order of $D_{\mathrm{V\ (450\ K)}} = 5\times10^{-37}$ m^2 s^{-1} [65]. With all other parameters being approximately the same for the nickel samples studied here (Eq. (1)), the expected relaxation times differ by at least two orders of magnitude between these two sample types. The accordingly reduced relaxation timescales in case of the HAGB specimens are reflected in their pronounced temperature dependence of mechanical properties, while the low diffusive, 'dense' TBs or LAGBs require higher temperatures to thermally activate such processes. This is reflected in their almost temperature-independent properties in the investigated temperature range, but also in activation enthalpies being comparable to bulk diffusion, compare Fig. 9b and Ref. [65]. The similar activation enthalpies calculated for the TBs and LAGBs is supported by simulation work, emphasizing that both, TBs and LAGBs, can provide easy slip transfer across the boundary, but can also resist dislocation slip. Except for the case of a screw dislocation impinging a TB, or a dislocation with proper Burgers vector impinging at the right position of the LAGB, locks or junctions are easily created. These sessile residuals of the interaction process may only be removed or overcome from subsequent dislocations by climb, necessitating in both cases a scenario close to bulk self-diffusion [89,94,95]. Similarly, although not as pronounced, the reduced diffusivity of HAGBs caused by alloying or impurities induces a shift towards higher testing temperatures until relaxation processes can be thermally activated. The reduction of V^* towards single digit values, found for the HAGB specimens once a pronounced temperature dependence of properties is measured (Fig. 8b), and the activation enthalpies being close to expectations for GB diffusion (compare Fig. 9b and Ref. [66]), further highlights the importance of diffusive processes at the GBs at these testing temperatures.

Thermally-induced stress relaxation at the boundaries thus not only explains the observed property differences between the three interface types, but also allows to rationalize the pronounced temperature dependent properties in case of the HAGB sample. In case of HAGBs, relaxation can occur at much smaller time scales, thus enhanced testing temperatures or prolonged testing times (i.e. reduction of the strain rate) already allow for diminishing stress fields. Their interaction with subsequent lattice dislocations is hence reduced and lower flow stresses are measured. Contrary the retarded relaxation at LAGBs or TBs, which occurs by dislocation climb [96], explains not only the reported higher work-hardening rates in this case [14–18], but also the rather temperature-invariant properties measured in Figs. 6 and 8. This interpretation is in line with recent investigations on NT copper suggesting that the rate limiting process is dislocation climb along the TBs, causing also an increase of the rate sensitivity at sufficiently high temperatures [88]. Since stress relaxation at GBs can also result in their migration, the observed grain growth beneath the indent of the HAGB samples well-below the thermal stability limit may not be too surprising (Fig. 7). Although frequently observed for nanostructures subjected to various loading situations (e.g. Refs. [36,53–55,97]), initiation of distinct grain growth by applying just 7% additional strain may appear intriguing at first view for a severely deformed sample. However, the equilibrium grain size was adjusted at RT, while HPT deformation at 418 K already yields an

increase of the minimum grain dimensions by 60% [98]. In addition to the increase of the testing temperature, the change of the loading situation itself could accelerate the migration rates [99]. Disconnections, GB line defects responsible for their migration [100–102], can also be generated by impinging lattice dislocations [100,103]. The step height and Burgers vector of the disconnection will, however, not only depend on boundary crystallography, but also on the interacting dislocation. Hence, a strain path change, activating different slip systems, could alter the active disconnection modes and accordingly the GB migration rates. The thermal and mechanical stability of a nanomaterial can thus largely differ, compare Figs. 3 and 6.

5. Summary and conclusions

The present results reveal a pronounced influence of the interface type on the deformation behavior of nanostructured nickel. Despite having a similar interfacial spacing, the presence of twin or low-angle boundaries results in an almost athermal behavior of hardness, rate sensitivity and activation volume. In contrast, the properties of HAGBs become strongly temperature-sensitive already at low homologous temperatures ($\geq 0.2\ T_m$), while alloying only induces a shift towards higher onset temperatures. These differences can be rationalized based on the important role of interfacial stress relaxation for the deformation behavior of nanomaterials and its dependence on boundary diffusivity. As observed for the HAGB specimens, interfacial stress release can distinctively modify the nanostructures tested. Noticeable grain growth below the thermal stability limit is reflected in a pronounced temperature dependence of hardness. These obvious differences induced by the interface type cannot be captured in predictions using models solely based on the interfacial spacing (i.e. modified Hall-Petch concepts). Hence, concepts including kinetics of accommodation and stress relaxation processes of dislocations at interfaces need to be targeted and developed to ensure more reliable property descriptions. While their kinetics are reasonably described for the pure thermally activated case, its stress dependence yet needs to be assessed. However, with future work in this field, a major step towards a generalized model capturing effects of chemistry, interface type or loading situation and, hence, a general prediction of mechanical properties of nanomaterials, seems accessible.

Declaration of Competing Interest

The authors declare that they have no known competing financial interests or personal relationships that could have appeared to influence the work reported in this paper.

Acknowledgments

Financial support by the European Research Council under ERC Grant Agreements No. 340185 USMS and No. 771146 TOUGHIT, the Austrian Academy of Sciences via the Innovation Fund IF 2019-37 and under the scope of the COMET program within the K2 Center 'Integrated Computational Material, Process and Product Engineering (IC-MPPE)' (Project No 859480) supported by the Austrian Federal Ministries for Climate Action, Environment, Mobility, Innovation and Technology (BMK) and for Digital and Economic Affairs (BMDW), represented by the Austrian research funding association (FFG), and the federal states of Styria, Upper Austria and Tyrol is gratefully acknowledged.

References

[1] M.A. Meyers, A. Mishra, D.J. Benson, Mechanical properties of nanocrystalline materials, Prog. Mater. Sci. 51 (2006) 427–556, doi:10.1016/j.pmatsci.2005.08.003.
[2] M. Dao, L. Lu, R.J. Asaro, J.T.M. De Hosson, E. Ma, Toward a quantitative understanding of mechanical behavior of nanocrystalline metals, Acta Mater. 55 (2007) 4041–4065, doi:10.1016/j.actamat.2007.01.038.
[3] Y. Li, D. Raabe, M. Herbig, P.P. Choi, S. Goto, A. Kostka, H. Yarita, C. Borchers, R. Kirchheim, Segregation stabilizes nanocrystalline bulk steel with near theoretical strength, Phys. Rev. Lett. 113 (2014) 106104, doi:10.1103/PhysRevLett.113.106104.
[4] J. Wang, Q. Zhou, S. Shao, A. Misra, Strength and plasticity of nanolaminated materials, Mater. Res. Lett. 5 (2017) 1–19, doi:10.1080/21663831.2016.1225321.
[5] H. Van Swygenhoven, P.M. Derlet, A.G. Frøseth, Nucleation and propagation of dislocations in nanocrystalline FCC metals, Acta Mater. 54 (2006) 1975–1983, doi:10.1016/j.actamat.2005.12.026.
[6] Q. Wei, S. Cheng, K.T. Ramesh, E. Ma, Effect of nanocrystalline and ultrafine grain sizes on the strain rate sensitivity and activation volume: FCC versus bcc metals, Mater. Sci. Eng. A. 381 (2004) 71–79, doi:10.1016/j.msea.2004.03.064.
[7] H.W. Höppel, J. May, P. Eisenlohr, M. Göken, Strain-rate sensitivity of ultrafine-grained materials, Zeitschrift Für Mater. Res. Adv. Technol. 96 (2005) 566–571, doi:10.1016/j.scriptamat.2005.03.043.
[8] H. Vehoff, D. Lemaire, K. Schüler, T. Waschkies, B. Yang, The effect of grain size on strain rate sensitivity and activation volume - from nano to ufg nickel, Int. J. Mater. Res. 98 (2007) 259–268, doi:10.3139/146.101464.
[9] O. Renk, V. Maier-Kiener, I. Issa, J.H. Li, D. Kiener, R. Pippan, Anneal hardening and elevated temperature strain rate sensitivity of nanostructured metals: their relation to intergranular dislocation accommodation, Acta Mater. 165 (2019) 409–419, doi:10.1016/j.actamat.2018.12.002.
[10] L. Lu, Y. Shen, X. Chen, L. Qian, K. Lu, Ultrahigh strength and high electrical conductivity in copper, Science 304 (2004) 422–426, doi:10.1126/science.1092905.
[11] K. Lu, L. Lu, S. Suresh, Strengthening materials by engineering coherent internal boundaries at the nanoscale, Science. 324 (2009) 349–352. doi:10.1126/science.1159610.
[12] Y.M. Wang, K. Wang, D. Pan, K. Lu, K.J. Hemker, E. Ma, Microsample tensile testing of nanocrystalline copper, Scr. Mater. 48 (2003) 1581–1586, doi:10.1016/S1359-6462(03)00159-3.
[13] S. Cheng, E. Ma, Y.M. Wang, L.J. Kecskes, K.M. Youssef, C.C. Koch, U.P. Trociewitz, K. Han, Tensile properties of in situ consolidated nanocrystalline Cu, Acta Mater. 53 (2005) 1521–1533, doi:10.1016/j.actamat.2004.12.005.
[14] L. Lu, M. Dao, T. Zhu, J. Li, Size dependence of rate-controlling deformation mechanisms in nanotwinned copper, Scr. Mater. 60 (2009) 1062–1066, doi:10.1016/j.scriptamat.2008.12.039.
[15] Z.X. Wu, Y.W. Zhang, D.J. Srolovitz, Dislocation-twin interaction mechanisms for ultrahigh strength and ductility in nanotwinned metals, Acta Mater. 57 (2009) 4508–4518, doi:10.1016/j.actamat.2009.06.015.
[16] M.J. Caturla, T.G. Nieh, J.S. Stolken, Differences in deformation processes in nanocrystalline nickel with low- and high-angle boundaries from atomistic simulations, Appl. Phys. Lett. 84 (2004) 598–600, doi:10.1063/1.1640464.
[17] P.L. Sun, C.Y. Yu, P.W. Kao, C.P. Chang, Influence of boundary characters on the tensile behavior of sub-micron-grained aluminum, Scr. Mater. 52 (2005) 265–269, doi:10.1016/j.scriptamat.2004.10.022.
[18] P.L. Sun, E.K. Cerreta, J.F. Bingert, G.T. Gray, M.F. Hundley, Enhanced tensile ductility through boundary structure engineering in ultrafine-grained aluminum, Mater. Sci. Eng. A. 464 (2007) 343–350, doi:10.1016/j.msea.2007.02.007.
[19] X.C. Liu, H.W. Zhang, K. Lu, Strain-induced ultrahard and ultrastable nanolaminated structure in nickel, Science 342 (2013) 337–340, doi:10.1126/science.1242578.
[20] Y. Zhao, T.A. Furnish, M.E. Kassner, A.M. Hodge, Thermal stability of highly nanotwinned copper: the role of grain boundaries and texture, J. Mater. Res. 27 (2012) 3049–3057, doi:10.1557/jmr.2012.376.
[21] X. Zhang, A. Misra, Superior thermal stability of coherent twin boundaries in nanotwinned metals, Scr. Mater. 66 (2012) 860–865, doi:10.1016/j.scriptamat.2012.01.026.
[22] Z.B. Wang, S.V. Divinski, Z.P. Luo, Y. Buranova, G. Wilde, K. Lu, Revealing interfacial diffusion kinetics in ultra-fine-laminated Ni with low-angle grain boundaries, Mater. Res. Lett. 5 (2017) 577–583, doi:10.1080/21663831.2017.1368036.
[23] M. Dao, L. Lu, Y.F. Shen, S. Suresh, Strength, strain-rate sensitivity and ductility of copper with nanoscale twins, Acta Mater. 54 (2006) 5421–5432, doi:10.1016/j.actamat.2006.06.062.
[24] P.H. Pumphrey, H. Gleiter, The annealing of dislocations in high-angle grain boundaries, Philos. Mag. 30 (1974) 593–602, doi:10.1080/14786439808206584.
[25] A.A. Nazarov, Kinetics of grain boundary recovery in deformed polycrystals, Interface Sci. 8 (2000) 315–322, doi:10.1023/A:1008720710330.
[26] L. Priester, Grain Boundaries From Theory To Engineering, 1st ed, Springer, Netherlands, 2013, doi:10.1007/978-94-007-4969-6.
[27] S.V. Divinski, G. Reglitz, H. Rösner, Y. Estrin, G. Wilde, Ultra-fast diffusion channels in pure Ni severely deformed by equal-channel angular pressing, Acta Mater. 59 (2011) 1974–1985, doi:10.1016/j.actamat.2010.11.063.
[28] Y.M. Wang, A.V. Hamza, E. Ma, Temperature-dependent strain rate sensitivity and activation volume of nanocrystalline Ni, Acta Mater. 54 (2006) 2715–2726, doi:10.1016/j.actamat.2006.02.013.
[29] J.R. Trelewicz, C.A. Schuh, Hot nanoindentation of nanocrystalline Ni-W alloys, Scr. Mater. 61 (2009) 1056–1059, doi:10.1016/j.scriptamat.2009.08.026.
[30] V. Maier, K. Durst, J. Mueller, B. Backes, H.W. Höppel, M. Göken, Nanoindentation strain-rate jump tests for determining the local strain-rate sensitivity in nanocrystalline Ni and ultrafine-grained Al, J. Mater. Res. 26 (2011) 1421–1430, doi:10.1557/jmr.2011.156.
[31] G. Mohanty, J.M. Wheeler, R. Raghavan, J. Wehrs, M. Hasegawa, S. Mischler, L. Philippe, J. Michler, Elevated temperature, strain rate jump microcompression of nanocrystalline nickel, Philos. Mag. 95 (2014) 1878–1895, doi:10.1080/14786435.2014.951709.
[32] A. Vorhauer, R. Pippan, On the onset of a steady state in body-centered cubic iron during severe plastic deformation at low homologous temperatures, Metall. Mater. Trans. A Phys. Metall. Mater. Sci. 39 (2008) 417–429, doi:10.1007/s11661-007-9413-1.
[33] Z.C. Wang, P.B. Prangnell, Microstructure refinement and mechanical properties

of severely deformed Al-Mg-Li alloys, Mater. Sci. Eng. A. 328 (2002) 87–97, doi:10.1016/S0921-5093(01)01681-1.
[34] P. Ghosh, O. Renk, R. Pippan, Microtexture analysis of restoration mechanisms during high pressure torsion of pure nickel, Mater. Sci. Eng. A 684 (2017) 101–109, doi:10.1016/j.msea.2016.12.032.
[35] F. Wetscher, R. Pippan, Cyclic high-pressure torsion of nickel and Armco iron, Philos. Mag. 86 (2006) 5867–5883, doi:10.1080/14786430600838288.
[36] M.W. Kapp, O. Renk, T. Leitner, P. Ghosh, B. Yang, R. Pippan, Cyclically induced grain growth within shear bands investigated in UFG Ni by cyclic high pressure torsion, J. Mater. Res. 32 (2017) 4317–4326, doi:10.1557/jmr.2017.273.
[37] B. Philippi, Aufbau Einer Anlage zur Gepulsten Elektrodeposition von Nanokristallinem Nickel, Saarland University, 2010.
[38] F.M. Kunz, Untersuchung des mikrostrukturellen Verhaltens Galvanisch Abgeschiedener Nanostrukturen unter äußeren Lasten, Saarland University, 2019.
[39] J.J. Fundenberger, E. Bouzy, D. Goran, J. Guyon, H. Yuan, A. Morawiec, Orientation mapping by transmission-SEM with an on-axis detector, Ultramicroscopy 161 (2016) 17–22, doi:10.1016/j.ultramic.2015.11.002.
[40] K. Durst, V. Maier, Dynamic nanoindentation testing for studying thermally activated processes from single to nanocrystalline metals, Curr. Opin. Solid State Mater. Sci. 19 (2015) 340–353, doi:10.1016/j.cossms.2015.02.001.
[41] J.M. Wheeler, D.E.J. Armstrong, W. Heinz, R. Schwaiger, High temperature nanoindentation: the state of the art and future challenges, Curr. Opin. Solid State Mater. Sci. 19 (2015) 354–366, doi:10.1016/j.cossms.2015.02.002.
[42] J.M. Wheeler, J. Michler, Elevated temperature, nano-mechanical testing *in situ* in the scanning electron microscope, Rev. Sci. Instrum. 84 (2013) 045103, doi:10.1063/1.4795829.
[43] W.C. Oliver, G.M. Pharr, Improved technique for determining hardness and elastic modulus using load and displacement sensing indentation experiments, J. Mater. Res. 7 (1992) 1564–1580, doi:10.1557/JMR.1992.1564.
[44] B.N. Lucas, W.C. Oliver, The elastic, plastic and time dependent properties of thin films as determined by ultra low load indentation, Mater. Res. Soc. Symp. Proc. 239 (1992) 337–341.
[45] P. Les, H.P. Stuewe, M. Zehetbauer, Hardening and strain rate sensitivity in stage IV of deformation in FCC and BCC Metals, Mater. Sci. Eng. A 234–236 (1997) 453–455, doi:10.1016/s0921-5093(97)00259-1.
[46] T. Hebesberger, H.P. Stüwe, A. Vorhauer, F. Wetscher, R. Pippan, Structure of Cu deformed by high pressure torsion, Acta Mater. 53 (2005) 393–402, doi:10.1016/j.actamat.2004.09.043.
[47] H.W. Zhang, X. Huang, N. Hansen, Evolution of microstructural parameters and flow stresses toward limits in nickel deformed to ultra-high strains, Acta Mater. 56 (2008) 5451–5465, doi:10.1016/j.actamat.2008.07.040.
[48] L.S. Toth, P. Gilormini, J.J. Jonas, Effect of rate sensitivity on the stability of torsion textures, Acta Metall. 36 (1988) 3077–3091, doi:10.1016/0001-6160(88)90045-4.
[49] P. Lejček, Grain boundary segregation in metals, Springer Ser. Mater. Sci. (2010) 1–36, doi:10.1007/978-3-642-12505-8_1.
[50] O. Renk, P. Ghosh, R. Pippan, From an understanding of structural restoration mechanisms towards a selective processing of extreme nanolamellar structures, in: Proceedings of the IOP Conference Series Materials Science and Engineering, 2017, p. 12037, doi:10.1088/1757-899X/219/1/012037.
[51] J. Wang, P.D. Hodgson, C. Yang, Effects of mechanical properties on the contact profile in Berkovich nanoindentation of elastoplastic materials, J. Mater. Res. 27 (2012) 313–319, doi:10.1557/jmr.2011.333.
[52] Y. Yee Lim, M M Chaudhri, The effect of the indenter load on the nanohardness of ductile metals: an experimental study on polycrystalline work-hardened and annealed oxygen-free copper, Philos. Mag. A 79 (1999) 2979–3000, doi:10.1080/014186199251193.
[53] K. Zhang, J.R. Weertman, J.A. Eastman, The influence of time, temperature, and grain size on indentation creep in high-purity nanocrystalline and ultrafine grain copper, Appl. Phys. Lett. 85 (2004) 5197–5199, doi:10.1063/1.1828213.
[54] M. Jin, A.M. Minor, E.A. Stach, J.W. Morris, Direct observation of deformation-induced grain growth during the nanoindentation of ultrafine-grained Al at room temperature, Acta Mater. 52 (2004) 5381–5387, doi:10.1016/j.actamat.2004.07.044.
[55] D.S. Gianola, S. Van Petegem, M. Legros, S. Brandstetter, H. Van Swygenhoven, K.J. Hemker, Stress-assisted discontinuous grain growth and its effect on the deformation behavior of nanocrystalline aluminum thin films, Acta Mater. 54 (2006) 2253–2263, doi:10.1016/j.actamat.2006.01.023.
[56] T.J. Rupert, D.S. Gianola, Y. Gan, K.J. Hemker, Experimental observations of stress-driven grain boundary migration, Science 326 (2009) 1686–1690, doi:10.1126/science.1178226.
[57] H. Mughrabi, H.W. Höppel, Cyclic deformation and fatigue properties of very fine-grained metals and alloys, Int. J. Fatigue 32 (2010) 1413–1427, doi:10.1016/j.ijfatigue.2009.10.007.
[58] D. Frazer, J.L. Bair, E.R. Homer, P. Hosemann, Cryogenic stress-driven grain growth observed via microcompression with in situ electron backscatter diffraction, JOM 72 (2020) 2051–2056, doi:10.1007/s11837-020-04075-x.
[59] K.L. Johnson, Contact Mechanics, Cambridge University Press, 1989, doi:10.1201/b17110-2.
[60] S. Harvey, H. Huang, S. Venkataraman, W.W. Gerberich, Microscopy and microindentation mechanics of single crystal Fe-3 wt. % Si: Part I. Atomic force microscopy of a small indentation, J. Mater. Res. 8 (1993) 1291–1299, doi:10.1557/JMR.1993.1291.
[61] S. Wierzbinski, A. Korbel, J.J. Jonas, Structural and mechanical aspects of high temperature deformation of polycrystalline nickel, Mater. Sci. Technol. U.K. 8 (1992) 153–158, doi:10.1179/mst.1992.8.2.153.
[62] C. Rehrl, S. Kleber, O. Renk, R. Pippan, Effect of forming conditions on the softening behavior in coarse grained structures, Mater. Sci. Eng. A 528 (2011) 6163–6172, doi:10.1016/j.msea.2011.04.043.
[63] D.H. Lee, I.C. Choi, G. Yang, Z. Lu, M. Kawasaki, U. Ramamurty, R. Schwaiger, J. il Jang, Activation energy for plastic flow in nanocrystalline CoCrFeMnNi high-entropy alloy: a high temperature nanoindentation study, Scr. Mater. 156 (2018) 129–133, doi:10.1016/j.scriptamat.2018.07.014.
[64] H. Conrad, Grain size dependence of the plastic deformation kinetics in Cu, Mater. Sci. Eng. A 341 (2003) 216–228, doi:10.1016/S0921-5093(02)00238-1.
[65] K. Maier, H. Mehrer, E. Lessmann, W. Schüle, Self-diffusion in nickel at low temperatures, Phys. Status Solidi. 78 (1976) 689–698, doi:10.1002/pssb.2220780230.
[66] S.V. Divinski, G. Reglitz, G. Wilde, Grain boundary self-diffusion in polycrystalline nickel of different purity levels, Acta Mater. 58 (2010) 386–395, doi:10.1016/j.actamat.2009.09.015.
[67] I.C. Choi, Y.J. Kim, Y.M. Wang, U. Ramamurty, J. Il Jang, Nanoindentation behavior of nanotwinned Cu: influence of indenter angle on hardness, strain rate sensitivity and activation volume, Acta Mater. 61 (2013) 7313–7323, doi:10.1016/j.actamat.2013.08.037.
[68] M. Winning, G. Gottstein, L.S. Shvindlerman, Stress induced grain boundary motion, Acta Mater. 49 (2001) 211–219, doi:10.1016/S1359-6454(00)00321-9.
[69] J. Kiely, J. Houston, Nanomechanical properties of Au (111), (001), and (110) surfaces, Phys. Rev. B Condens. Matter Mater. Phys. 57 (1998) 12588–12594, doi:10.1103/PhysRevB.57.12588.
[70] R. Smith, D. Christopher, S.D. Kenny, A. Richter, B. Wolf, Defect generation and pileup of atoms during nanoindentation of Fe single crystals, Phys. Rev. B Condens. Matter Mater. Phys. 67 (2003), doi:10.1103/PhysRevB.67.245405.
[71] S. Jakob, A. Leitner, A. Lorich, M. Eidenberger-Schober, W. Knabl, R. Pippan, H. Clemens, V. Maier-Kiener, Influence of crystal orientation and Berkovich tip rotation on the mechanical characterization of grain boundaries in molybdenum, Mater. Des. 182 (2019), doi:10.1016/j.matdes.2019.107998.
[72] Z. You, X. Li, L. Gui, Q. Lu, T. Zhu, H. Gao, L. Lu, Plastic anisotropy and associated deformation mechanisms in nanotwinned metals, Acta Mater. 61 (2013) 217–227, doi:10.1016/j.actamat.2012.09.052.
[73] M.W. Kapp, A. Hohenwarter, S. Wurster, B. Yang, R. Pippan, Anisotropic deformation characteristics of an ultrafine- and nanolamellar pearlitic steel, Acta Mater. 106 (2016) 239–248, doi:10.1016/j.actamat.2015.12.037.
[74] C.R. Mayer, L.W. Yang, S.S. Singh, J. Llorca, J.M. Molina-Aldareguia, Y.L. Shen, N. Chawla, Anisotropy, size, and aspect ratio effects on micropillar compression of Al[sbnd]SiC nanolaminate composites, Acta Mater. 114 (2016) 25–32, doi:10.1016/j.actamat.2016.05.018.
[75] Y.P. Li, X.F. Zhu, J. Tan, B. Wu, W. Wang, G.P. Zhang, Comparative investigation of strength and plastic instability in Cu/Au and Cu/Cr multilayers by indentation, J. Mater. Res. 24 (2009) 728–735, doi:10.1557/jmr.2009.0092.
[76] Y.P. Li, X.F. Zhu, G.P. Zhang, J. Tan, W. Wang, B. Wu, Investigation of deformation instability of Au/Cu multilayers by indentation, Philos. Mag. 90 (2010) 3049–3067, doi:10.1080/14786431003776802.
[77] D. Bhattacharyya, N.A. Mara, P. Dickerson, R.G. Hoagland, A. Misra, Transmission electron microscopy study of the deformation behavior of Cu/Nb and Cu/Ni nanoscale multilayers during nanoindentation, J. Mater. Res. 24 (2009) 1291–1302, doi:10.1557/jmr.2009.0147.
[78] A. Seeger, CXXXII. The generation of lattice defects by moving dislocations, and its application to the temperature dependence of the flow-stress of FCC crystals, London, Edinburgh, Dublin Philos. Mag, J. Sci. 46 (1955) 1194–1217, doi:10.1080/14786441108520632.
[79] P.B. Hirsch, D.H. Warrington, The flow stress of aluminium and copper at high temperatures, Philos. Mag. 6 (1961) 735–768, doi:10.1080/14786436108238367.
[80] R.P. Carreker, W.R. Hibbard, Tensile deformation of high-purity copper as a function of temperature, strain rate, and grain size, Acta Metall. (1953) 1, doi:10.1016/0001-6160(53)90022-4.
[81] Y.M. Wang, E. Ma, On the origin of ultrahigh cryogenic strength of nanocrystalline metals, Appl. Phys. Lett. 85 (2004) 2750–2752, doi:10.1063/1.1799238.
[82] R.S. Mishra, V.V. Stolyarov, C. Echer, R.Z. Valiev, A.K. Mukherjee, Mechanical behavior and superplasticity of a severe plastic deformation processed nanocrystalline Ti-6Al-4V alloy, Mater. Sci. Eng. A. 298 (2001) 44–50, doi:10.1016/s0921-5093(00)01338-1.
[83] Y. Champion, Y. Br??chet, Effect of grain size reduction and geometrical confinement in fine grained copper: Potential applications as a material for reversible electrical contacts, Adv. Eng. Mater. 12 (2010) 798–802, doi:10.1002/adem.200900346.
[84] M.A. Monclús, M. Karlik, M. Callisti, E. Frutos, J. Llorca, T. Polcar, J.M. Molina-Aldareguía, Microstructure and mechanical properties of physical vapor deposited Cu/W nanoscale multilayers: Influence of layer thickness and temperature, Thin Solid Films (2014) 275–282, doi:10.1016/j.tsf.2014.05.044.
[85] J. Snel, M.A. Monclús, M. Castillo-Rodríguez, N. Mara, I.J. Beyerlein, J. Llorca, J.M. Molina-Aldareguía, Deformation mechanism map of Cu/Nb nanoscale metallic multilayers as a function of temperature and layer thickness, JOM 69 (2017) 2214–2226, doi:10.1007/s11837-017-2533-1.
[86] A.A. Volinsky, N.R. Moody, W.W. Gerberich, Nanoindentation of Au and Pt/Cu thin films at elevated temperatures, J. Mater. Res. 19 (2004) 2650–2657, doi:10.1557/JMR.2004.0331.
[87] Q. Lu, Z. You, X. Huang, N. Hansen, L. Lu, Dependence of dislocation structure on orientation and slip systems in highly oriented nanotwinned Cu, Acta Mater 127 (2017) 85–97, doi:10.1016/j.actamat.2017.01.016.
[88] L.W. Yang, C.Y. Wang, M.A. Monclús, L. Lu, J.M. Molina-Aldareguía, J. Llorca, Influence of temperature on the strain rate sensitivity and deformation mechanisms of nanotwinned Cu, Scr. Mater. 154 (2018) 54–59, doi:10.1016/j.scriptamat.2018.05.018.

[89] Y. Gao, Z. Jin, Interactions between lattice dislocation and Lomer-type low-angle grain boundary in nickel, Comput. Mater. Sci. 138 (2017) 225–235, doi:10.1016/j.commatsci.2017.06.025.
[90] D.W. Adams, D.T. Fullwood, R.H. Wagoner, E.R. Homer, Atomistic survey of grain boundary-dislocation interactions in FCC nickel, Comput. Mater. Sci. 164 (2019) 171–185, doi:10.1016/j.commatsci.2019.04.007.
[91] D. Hull, D.J. Bacon, Introduction to dislocations, 2011. doi:10.1016/C2009-0-64358-0.
[92] F. Mompiou, D. Caillard, M. Legros, H. Mughrabi, In situ TEM observations of reverse dislocation motion upon unloading in tensile-deformed UFG aluminium, Acta Mater. 60 (2012) 3402–3414, doi:10.1016/j.actamat.2012.02.049.
[93] H. Mehrer, Diffusion in Solids: Fundamentals, Methods, Materials, Diffusion-Controlled Processes, Springer Series in Solid-State Sciences, 2007, doi:10.1007/978-3-540-71488-0.
[94] Z. Zhang, C. Shao, S. Wang, X. Luo, K. Zheng, H.M. Urbassek, Interaction of dislocations and interfaces in crystalline heterostructures: a review of atomistic studies, Crystals (2019) 9, doi:10.3390/cryst9110584.
[95] B. Liu, P. Eisenlohr, F. Roters, D. Raabe, Simulation of dislocation penetration through a general low-angle grain boundary, Acta Mater. 60 (2012) 5380–5390, doi:10.1016/j.actamat.2012.05.002.
[96] Y. Gu, Y. Xiang, D.J. Srolovitz, Relaxation of low-angle grain boundary structure by climb of the constituent dislocations, Scr. Mater. 114 (2016) 35–40, doi:10.1016/j.scriptamat.2015.11.016.
[97] S. Brandstetter, K. Zhang, A. Escuadro, J.R. Weertman, H. Van Swygenhoven, Grain coarsening during compression of bulk nanocrystalline nickel and copper, Scr. Mater. 58 (2008) 61–64, doi:10.1016/j.scriptamat.2007.08.042.
[98] O. Renk, R. Pippan, Transition from thermally assisted to mechanically driven boundary migration and related apparent activation energies, Scr. Mater. 154 (2018) 212–215, doi:10.1016/j.scriptamat.2018.05.052.
[99] O. Renk, P. Ghosh, R.K. Sabat, J. Eckert, R. Pippan, The role of crystallographic texture on mechanically induced grain boundary migration, Acta Mater. 200 (2020) 404–416, doi:10.1016/j.actamat.2020.08.071.
[100] A. Rajabzadeh, F. Mompiou, S. Lartigue-Korinek, N. Combe, M. Legros, D.A. Molodov, The role of disconnections in deformation-coupled grain boundary migration, Acta Mater. 77 (2014) 223–235, doi:10.1016/j.actamat.2014.05.062.
[101] J. Han, S.L. Thomas, D.J. Srolovitz, Grain-boundary kinetics: A unified approach, Prog. Mater. Sci. 98 (2018) 386–476, doi:10.1016/j.pmatsci.2018.05.004.
[102] Q. Zhu, G. Cao, J. Wang, C. Deng, J. Li, Z. Zhang, S.X. Mao, In situ atomistic observation of disconnection-mediated grain boundary migration, Nat. Commun. 10 (2019) 156, doi:10.1038/s41467-018-08031-x.
[103] N. Kvashin, P.L. Garc'ia-Müller, N. Anento, A. Serra, Atomic processes of shear-coupled migration in {112} twins and vicinal grain boundaries in BCC-Fe, Phys. Rev. Mater. 4 (2020) 73604, doi:10.1103/PhysRevMaterials.4.073604.